(Preprint) AAS 25-151

PASSIVE POTENTIAL SENSING IN CISLUNAR SPACE: SIMULATIONS USING NASCAP-2K AND SPIS

Kaylee Champion*and Hanspeter Schaub †

Spacecraft interact with the ambient plasma environment and develop surface potentials, which can cause arc discharges during docking, coulomb torques during proximity operations, or be utilized for electrostatic actuation. To manage the effects of spacecraft charging during proximity operations, the neighboring spacecraft potential must be known. The electron emissions from a target, naturally generated by the ambient plasma environment, can be measured by a nearby servicing spacecraft to determine the target's potential. This technology has been investigated for application in Geosynchronous space and may be extended to cislunar space. In cislunar space, spacecraft plasma interactions such as wakes and non-monotonic sheaths may complicate sensing. Therefore, simulations are conducted in Nascap-2k and SPIS to determine when wakes and non-monotonic sheaths are expected to form and their impact on sensing. It is shown that wakes and non-monotonic sheaths restrict electron emissions from leaving a target if the spacecraft width is at least 80% of the electron Debye length and sufficient electrons are emitted. Furthermore, non-monotonic sheaths disappear when a positive servicer is placed next to the target, but the servicer's wake cause the target to charge more negatively and severely limit the target's electron emission current.

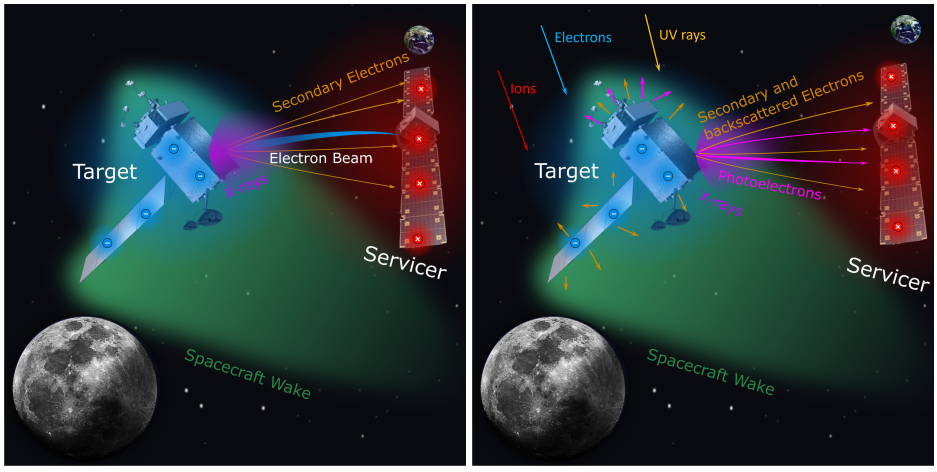

(a) Active sensing (b) Passive sensing

Figure 1. Active and passive touchless potential sensing of a neighboring spacecraft in cislunar space

*Graduate Research Assistant, Department of Aerospace Engineering Sciences, University of Colorado Boulder, CO, United States. AIAA student member.email:kaylee.champion@colorado.edu

†Distinguished Professor and Department Chair, Schaden Leadership Chair, Glenn L. Murphy Chair in Engineering, Ann and H.J. Smead Aerospace Engineering Sciences, AIAA and AAS Fellow.

INTRODUCTION

Spacecraft are exposed to the ambient plasma and radiation environment, generating surface currents and potentials through a process referred to as spacecraft charging. The magnitude of the surface potential is dependent on the local plasma parameters, sunlit surface area, material properties, and spacecraft geometry.[1] Thus, two spacecraft or electrically disconnected surfaces may charge differently in the same space environment. If the difference in potentials between two spacecraft surfaces is sufficiently large, an arc discharge can occur, frying components and potentially ending the mission.[2–6] This is dangerous during docking, particularly if one spacecraft is in the shadow of the other, as eclipsed spacecraft typically charge more negative than sunlit craft.[7–9] In addition, charged spacecraft exert electrostatic forces and torques on each other during proximity operations, which introduces unexpected perturbations that can require extra maneuvers and fuel to counteract.[10] Conversely, the electrostatic force can be used for touchless applications such as moving space debris, detumbling a target, and assisting with docking.[11–15] This is referred to as electrostatic actuation.

Knowledge of a nearby object's potential is critical for mitigating the dangerous effects of spacecraft charging or enabling electrostatic actuation. Touchless potential sensing techniques have been investigated to determine the potential of a neighboring spacecraft in Geosynchronous (GEO) and cislunar environments. Active methods of touchless potential sensing involve a servicing spacecraft aiming an electron beam at a target spacecraft to excite secondary electron (SE)[16–19] and x-ray emissions,[20–22] or an ultraviolet (UV) laser to excite photoelectron emissions.[23] Passive methods rely on the x-ray and electron emissions naturally excited by the environment.[16,24] Passive potential sensing is useful when active sensing methods may cause damage to sensitive components or induce unwanted charging. The energy of the emissions are measured by the servicer and used to determine the potential of the target with respect to the servicer (Figure 1). The servicer can determine its own potential using existing tools,[25–27] and the potential of the target is inferred.

Most touchless potential sensing research has been conducted assuming GEO-like plasma conditions. In recent years, worldwide enthusiasm for cislunar space has led to an increased number of missions, including Intuitive Machine's Odysseus spacecraft, India's Chandrayaan-3 lander,[28] China's Change'E-6 spacecraft,[29] and Japan's SLIM spacecraft.[30] Lunar Gateway is also currently being constructed by multiple partners around the globe and will provide a sustained human presence around the moon.[31] With more spacecraft and cislunar proximity operations, touchless potential sensing should be extended to cislunar space to minimize the chances of arcing during docking procedures and account for electrostatic forces and torques.

Spacecraft-plasma interactions are expected around the moon that have not been encountered in GEO, including shorter Debye lengths, spacecraft wakes, and non-monotonic sheaths. While touchless sensing has been shown to be feasible despite short Debye lengths, prior work has not addressed the effects of wakes or non-monotonic sheath formations.[32] Therefore, it is necessary to conduct further investigations to understand how these phenomena impact touchless potential sensing.

This work aims to determine the conditions under which spacecraft wakes and non-monotonic sheaths form around moon-orbiting spacecraft and their impact on electron emissions used for passive potential sensing. To achieve this, simulations are conducted in spacecraft-plasma interactions software. The environments applied to the simulations and expected spacecraft-plasma interactions are first described, followed by characterization of wake and sheath formations around a single

spacecraft in cislunar space. Next, passive potential sensing simulations are conducted with two spacecraft to determine how the presence of a servicer changes wake and sheath formations and to identify the ideal position for the servicer with respect to the target for detecting electron emissions. Last, an overview of the findings and conclusions are presented.

CISLUNAR ENVIRONMENT AND INTERACTIONS

The moon orbits through Earth's magnetosphere and out into the flowing solar wind, passing through a range of plasma environments. Several missions have helped characterize the cislunar plasma environments, including the Apollo missions,[33–35] the Wind spacecraft,[36] the Lunar Reconnaissance Orbiter (LRO),[37] and the twin Acceleration, Reconnection, Turbulence, and Electrodynamics of the Moon's Interaction with the Sun (ARTEMIS) spacecraft.[38] Measurements from the ARTEMIS spacecraft are analyzed and binned in the *Design Specification for the Natural Environment* (DSNE) document produced by NASA,[39] which identifies four plasma regions: solar wind, magnetosheath, magnetotail lobes, and plasmasheet (Figure 2(a)). The plasma in the solar wind and magnetosheath is less energetic and more dense than the plasma in the plasmasheet and magnetotail lobes. In addition to orbiting through several regions, the moon alters the ambient plasma. In the solar wind and magnetosheath, the moon absorbs and reflects plasma, leaving a low density, complex structure on the eclipse side of the moon, known as the lunar wake (Figure 2(b)).[40]

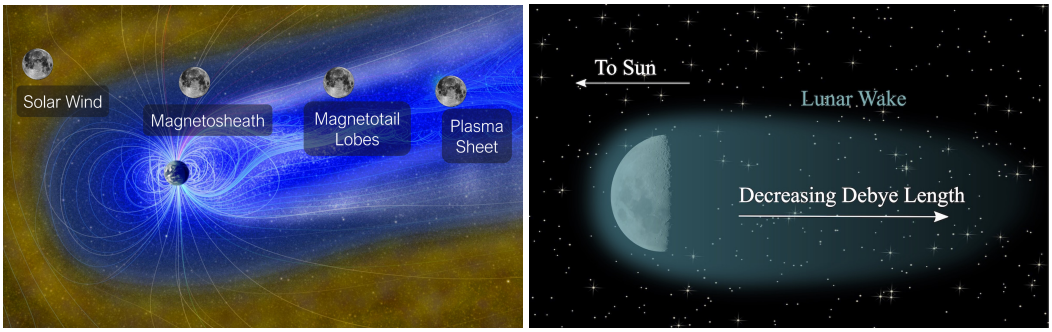

(a) Cislunar Environments (b) Lunar wake

Figure 2. Lunar plasma environments and interactions[32]

In addition to the moon altering the ambient plasma environment, the spacecraft interact with the plasma as they move through it. This disturbing the ambient electrons and ions, moving them out of the way. In hot plasma environments, the ions and electrons catch back up and impact all sides of the spacecraft. In less energetic plasma environments, the ion thermal velocity v_i is less than the velocity of the spacecraft v_{sc} while the electron thermal velocity v_e is higher than the spacecraft velocity making the spacecraft mesothermal with respect to the plasma ($v_i < v_{sc} < v_e$). Under these conditions, it may take several spacecraft lengths for the ions to catch back up, leaving a complex ion void region known as a spacecraft wake on the anti-velocity side of the spacecraft and a high density ion region on the ram side.[1] Spacecraft wakes have been investigated numerically to understand wake formations about spacecraft with large potentials,[41–43] their impact on surface charging,[7,44,45] and their effects on scientific instruments.[46,47] Spacecrafts wakes have also been generated in vacuum chamber experiments to determine their properties,[48–52] characterize how wakes alter space plasma measurements,[53,54] and even investigate the effects of lunar wakes on regolith charging.[55]

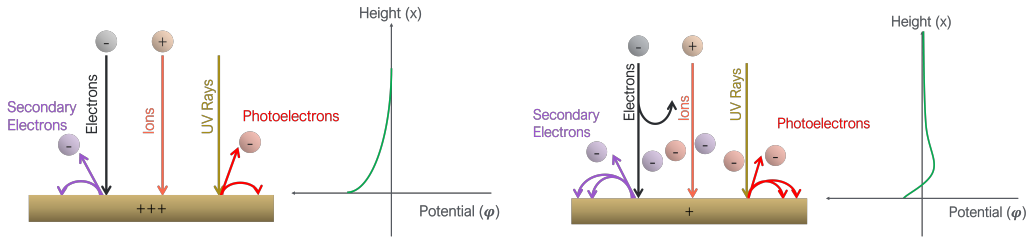

(a) Monotonic (b) Non-monotonic

Figure 3. Schematic of monotonic and non-monotonic sheath formation for a sunlit spacecraft.

Spacecraft wakes are expected in the solar wind and magnetosheath dayside regions.[56] On the dayside of the moon, the wake formation remain relatively consistent for varying spacecraft altitudes. On the eclipse side, spacecraft wakes are smaller near the surface, but as the craft's altitude increases the wakes grow and eventually resemble the dayside wakes. Because wakes are mostly void of ions, an object in the wake of another spacecraft can experience extreme charging, which increases the risk of electrostatic arc discharges during docking operations.[7] Furthermore, the negative potential field in the wake can deflect electrons, adding further complexity to touchless potential sensing.[44,57–59]

In a typical spacecraft sheath, the potential field decreases monotonically from the spacecraft surface value to zero as the distance from the surface increases. In this scenario, low energy electron emissions, such as secondary electron and photoelectron emissions, may return to the surface if the spacecraft is positively charged, as shown in Figure 3(a). Conversely, if the spacecraft is charged negatively, the electron emissions should be repelled from the spacecraft surface.

When electrons are emitted, their negative charge reduces the ambient potential field. If the ratio of emitted electrons to incoming electrons (Γ) is above some critical value (Γ_c) the electron emissions can settle close to the spacecraft surface, causing the potential field to dip below the spacecraft surface potential. This dip in the potential field creates a non-monotonic sheath, as illustrated for a sunlit spacecraft in Figure 3(b). Non-monotonic sheath can also form about a negative, eclipsed spacecraft due to secondary electron emissions. The non-monotonic sheath is also referred to as a barrier because it can prevent low energy electron emissions from leaving the spacecraft surface, effectively reducing the emitted electron yield. While low-energy ambient electrons are repelled, the current change is minimal compared to the effect on electron emissions.

In addition to having a large emitted to incoming electron ratio, the spacecraft size must be comparable to or larger than the photoelectron λ_{ph} and electron λ_D Debye lengths for non-monotonic sheaths to form. The Debye length is a measure of how far a charged particle's electrostatic effect persists, and in a Maxwellian plasma is given by

$$\lambda = \sqrt{\frac{\epsilon_0 T_e}{n_e q_e}}, \tag{1}$$

where ϵ_0 is the permittivity of free space, T_e is the electron temperature in eV, q_e is the elementary charge, and n_e is the electron density. The photoelectron Debye length is typically much smaller than the electron Debye length and dominates near the spacecraft surface, while the electron Debye length dominates farther from the spacecraft.

If the spacecraft is comparable in size to the electron Debye length and much larger than the photoelectron Debye length, the "thin sheath" approximation applies. In this regime, a non-monotonic sheath creates a potential barrier close to the spacecraft that prevents electron emissions from leaving the target. The spacecraft could then be negatively charged even with a large electron emission currents. If the spacecraft is smaller than the Debye length, the "thick sheath" approximation applies, and the barriers effectively disappear. In this regime, recollection of electron emissions is driven by positive surface potentials attracting emitted electrons.

Non-monotonic sheaths have been investigated both analytically and numerically to determine their impact on spacecraft charging,[57,58,60] measurements,[61,62] and lunar surface charging.[63–65] Experimental results have validated their formation,[66,67] and they have been observed above the dayside lunar surface.[68] For touchless potential sensing, if barriers prevent electron emissions from leaving the target, they cannot reach the servicer to be sensed.

SIMULATION SETUP

The simulations are conducted in Nascap-2k and Spacecraft Plasma Interactions Software (SPIS). Nascap-2k is a spacecraft charging and plasma interactions code developed as a collaboration between NASA and the Air Force Research Lab.[69] SPIS is a spacecraft plasma interaction software created by the Spacecraft Plasma Interactions Network in Europe (SPINE).[70] While both programs aim to solve similar problems, their underlying processes and assumptions vary. So, using both programs validates the results of both programs and provides a reasonable range of expected interactions.

Current Sources

In Nascap-2k and SPIS, the potential is determined by solving the current balance equation

$$I_i(1+\delta_i) + I_e(1-(\eta+\delta)) + I_{ph} = 0, \tag{2}$$

where I_i and I_e are the incident ion and electron currents, respectively, and I_{ph} is the photoelectron current. The variables η, δ, and δ_i are the backscattered, secondary electrons from electrons and secondary electrons from ions yields, respectively. For all scenarios, the ions are assumed to be H^+, and the surface material is **aluminum**. The ion and electron currents are handled differently in each program and are described in the following sections. The yields are defined the same in Nascap-2k and SPIS and can be found in Nascap-2k's *Scientific Documentation*.[71] The photoelectron and secondary electron current are utilized for touchless potential sensing, so they are described here for convenience.

The secondary electron yield δ is defined using a four parameter fit

$$\delta(E) = R_1 E^{e_1} + R_2 E^{e_2}, \tag{3}$$

where R_1, R_2, e_1, and e_2 are unit-less inputs used when defining the material. The fitting parameters are 154, 330, 0.8, and 1.76 for R_1, R_2, e_1, and e_2, respectively. The maximum yield δ_{max} and electron energy at which the maximum yield occurs E_{max} are 0.97 and 300 eV, respectively.

The photoelectron current density J_{ph} at 1 AU is defined as 4E-5 A/m^2. The photoelectron number density n_{ph} is

$$n_{ph} = \frac{2J_{ph}}{q_e v_{ph}}, \tag{4}$$

where $v_{ph} = \sqrt{2q_eT_{ph}/(\pi m_e)}$ is the photoelectron velocity, m_e is the mass of an electron in kg, and T_{ph} is the photoelectron temperature. Both photoelectron and secondary electron emissions are assumed to have an energy of 2 eV and a Maxwellian distribution on the surface of the spacecraft. The photoelectron number density is then approximately 1054 cm^{-3}, and the photoelectron Debye length λ_{ph} is 0.32 m.

Nascap-2k

The computational space in Nascap-2k is defined using a Cartesian grid. The size of the domain, or external boundary, and resolution at the boundary are specified by the *primary grid*. The external boundary is set sufficiently far from the spacecraft so that the entire potential sheath is contained in the simulation. This is typically at least three Debye lengths. The potential field is at the boundary is fixed at 0 V (Dirichlet boundary condition). The grid size at the boundary is 10 m or less, with finer resolution used in regions with shorter Debye lengths. Closer to the spacecraft, the resolution is defined using *child grids*. Near the surface of the spacecraft, the grids should be smaller than the photoelectron Debye length. The child grid element around the spacecraft are set to 0.2 m, as decreasing the size to 0.1 m shows negligible change in the results and significantly increases the computational time.

Once the object and grids are defined, parameters are configured on the various tabs in Nascap-2k. In the *Problem* tab, the "Interplanetary" environment is selected, surface currents are solved using "Tracked Ion and Analytic Electrons", and the potentials in space are found using the "Self-consistent with Ion Trajectories" option. For these options, ions particles are tracked, and electrons are represented using appropriate analytic equations, as electron tracking is unavailable in the interplanetary environment. In the *Particles* tab, the ions are injected from the boundary, and under *Advanced* options, the fraction of distribution is split 0.1, 0.4, 0.4, 0.1 in the directions perpendicular to the spacecraft velocity and 0.3, 0.4, 0.3 parallel to the flow, following the recommendation in Reference 72. Once the parameters are configured, the script is built and run. Simulations typically take one to eight hours to run.

SPIS

In SPIS, The computational space is defined using a tetrahedral mesh created in Gmsh and loaded directly into the *Mesh* tab. The outer boundary is again placed far enough away to contain the entire sheath, and the resolution is 0.2 m on the spacecraft surfaces and 10 m or less at the boundary. Changing the mesh size on the spacecraft surface to 0.1 m again shows negligible difference in results while significantly increasing the computational time.

A Dirichlet boundary condition of 0 V is again applied at the boundaries, and open boundaries are defined for the particles, which means particles can be injected and lost through the surface. The electrons and ions are modeled using the particle-in-cell (PIC) option, where macroparticles are generated and tracked throughout the computational space. All electron emissions are also modeled with PIC to capture the complex dynamics near the spacecraft surface. The maximum integration time for all particles is set to 1E-6 s. Surface currents are found by summing the particle impacts and emissions, and the non-linear Poisson equation determines the electric field. When conducting PIC simulations, the time-steps must be small enough to ensure stability and smooth convergence.[72] The spacecraft typically reaches a steady state between 1E-4 and 5E-3 seconds, and the maximum time step is between 1E-6 and 1E-5 seconds. The simulation run time is between three to twelve hours.

Table 1. Sunlit environments based on the DSNE, and spacecraft charging results.

Environment	Particle Density (m^{-3})	Electron Temp. (eV)	Ion Velocity (km/s)	Ion Temp. (eV)	Debye Length (m)	Nascap Pot. (V)	SPIS Pot. (V)	Nascap I_{ph} (μA)	SPIS I_{ph} (μA)
Magnetotail Lobes	2E5	48	170	290	115.2	10.2	13.7	1	1
Plasma Sheet	2.2E5	150	110	780	194.1	9.7	12.5	1.2	1
Magnetosheath Dayside	9.5E6	18	350	94	10.2	3.5	6.3	27	28
Solar Wind Dayside	6E6	11	420	7	10.1	4.4	7.5	18	20

SINGLE SPACECRAFT CHARACTERIZATION

Simulations with a single spacecraft are first conducted to determine the conditions in which spacecraft wakes and non-monotonic sheaths form around moon-orbiting spacecraft. The environmental parameters are based on the average values in the DNSE.[39] However, in some environments, the ion n_i and electron n_e densities differ, creating a non-neutral plasma that is incompatible with the Dirichlet boundary condition.Currently, there is no solution for this in spacecraft-plasma interaction codes, so typically the ion density is set equal to the electron density. To ensure this is a reasonable solution, simulations are run in Nascap-2k to determine how changing the ion density alters the results. In Nascap-2k, the spacecraft charge and currents can be determined using "Analytic Currents", which does not require a grid or equal electron and ion density. Simulations are first conducted for a 2 m wide aluminum cube in the solar wind wake environment with n_i set as specified in the DSNE. Then the simulations are repeated with $n_i = n_e$. When the ion density is changed, the spacecraft potential changes by approximately 10%.

Next, the solution method is changed from "Analytic Currents" to "Tracked Ion and Analytic Electrons" with a grid and $n_i = n_e$. This change increases the surface potential variation by approximately 21% compared to the analytic solution with $n_i = n_e$. These findings indicate that the variations introduced by changing the solution method are larger than those caused by altering ion density. It cannot be said which solution method is the most correct, so the results show that the error from assuming $n_i = n_e$ is smaller than the inherent uncertainty in spacecraft-plasma interaction software. Therefore, the solutions are considered representative.

Sunlit Spacecraft

A 2 m wide aluminum cube is first modeled in the average sunlit environments using both Nascap-2k and SPIS. In these environments, the photoelectron current I_{ph} is highest, making it ideal for passive touchless potential sensing and typically causing spacecraft to charge a few volts positive. The final photoelectron current shown in the last two columns in Table 1 represents the emitted photoelectron current minus the recollected current. Because the spacecraft here is much smaller than all the electron Debye lengths, potential barriers do not form, and recollection of electron emissions is entirely due to the positive spacecraft potential. Despite the fact that the majority of the photoelectron current is recaptured, the photoelectron current remains on the same order as the collected electron current. This is promising for touchless potential sensing, as the servicer must be able to distinguish the electrons emitted from the target from the electrons in the environment.

Previous work has shown that barriers form as a spacecraft transitions from cislunar space to the

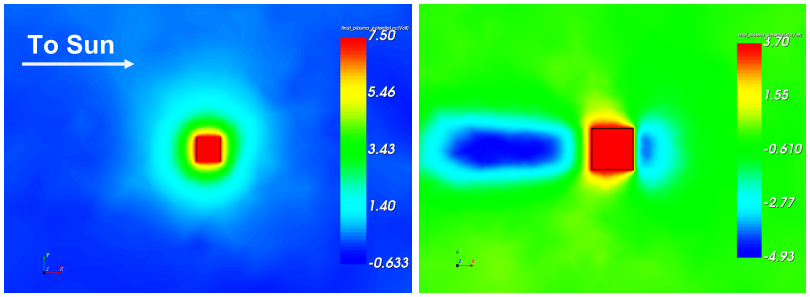

(a) 2 m SC potential field (b) 20 m SC potential field

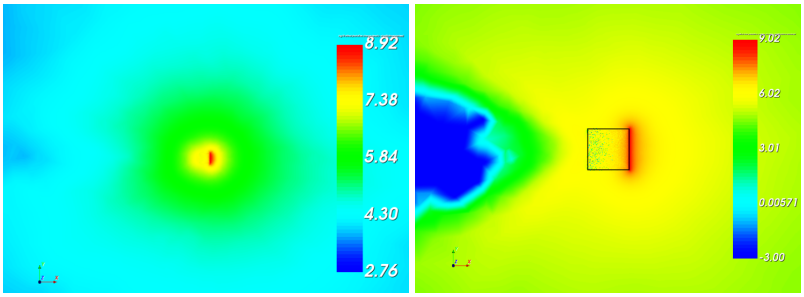

(c) 2 m SC $\log_{10}(n_{ph})$ (d) 20 m SC $\log_{10}(n_{ph})$

Figure 4. The potential field (top) and $\log_{10}$ of the photoelectron density n_{ph} (bottom) of a 2 m (left) and 20 m (right) spacecraft in solar wind dayside plasma (λ_D=10.1 m)

near Sun environment due to decreasing Debye length.[57,59] These investigated utilize a spacecraft with a constant width, so the impact of spacecraft size on barrier formation near the moon has not been explored. To address this, spacecraft of varying widths are simulated in the solar wind dayside environment to determine the spacecraft size to electron Debye length in which barriers could form. SPIS is used for this analysis because Nascap-2k's analytic representation of electrons does not capture non-monotonic sheath formations. In other words, Nascap-2k is suitable for cases without barriers, or the thick sheath regime.

Figure 4 shows the potential fields and photoelectron trajectories for a 2 m and 20 m wide spacecraft. The potential field around the 2 m spacecraft drops monotonically to zero, and the photoelectron emissions forming a sheath around the entirety of the spacecraft. In contrast, potential dips form around the 20 m spacecraft. The dip on the sunlit side forms due to the photoelectron barrier, while the dip on the wake side forms due to the spacecraft wake. The photoelectrons begin to form a sheath around the spacecraft, but the negative potentials in the wake prevent them from accumulating on the eclipse side of the spacecraft.

The resulting potential fields and fraction of electron emissions that are recollected are shown in Figure 5. As the spacecraft width increases, the system transitions from the thick sheath regime to the thin sheath regime, increasing the fraction of electron emission recollected and decreasing the spacecraft potential.On the sunlit side (positive x-values), the potential barrier forms due to the high density of photoelectron emissions. Once the spacecraft is 8 m wide (a spacecraft width to electron Debye length ratio ρ of 0.79), a clear barrier forms on the sunlit side, and the spacecraft can be considered in the thin sheath regime.

On the eclipse side (negative x-values), a barrier forms due to the negative potential in the space-

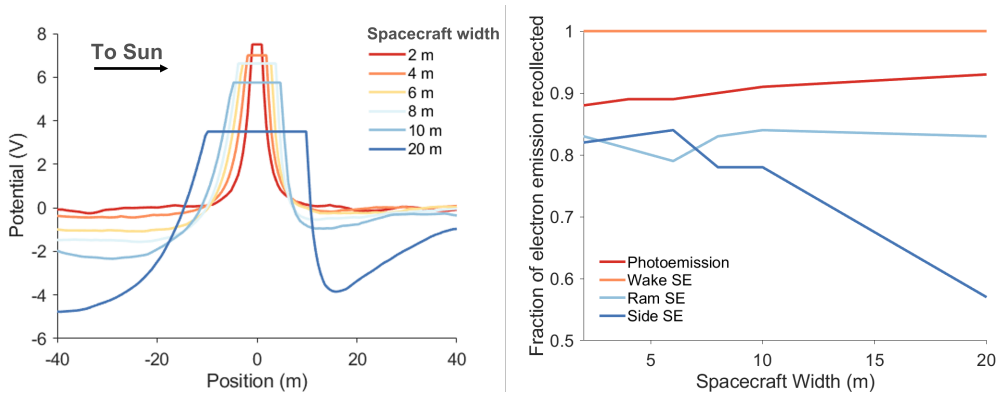

(a) Potential fields

(b) Fraction of current recollected

Figure 5. Potential field (left) and fraction of electron emissions recollected (right) for spacecraft of varying widths in Solar Wind dayside plasma (λ_D=10.1).

craft wake. In the thick sheath regime, the negative charge in the wake minimally changes the potential field, and electrons are recollected due to the spacecraft's positive potential. Once the spacecraft width reaches 6 m ($\rho \approx 0.59$), the wakes negative charge creates a distinct potential barrier. The minimum potential is more negative in the wake than the photoelectron barrier, leading to the secondary electrons being completely recollected on the wake side. This could limit the possibility of a servicer determining the target's potential when positioned in its wake.

Eclipse Spacecraft

A 2 m aluminum spacecraft is then simulated in the eclipse cislunar environments, where the secondary electron current is the dominant electron emission current and is utilized to determine the target's potential. Figure 6 shows the secondary electron currents from the ram, wake, and side of the spacecraft. SPIS consistently predicts the highest current on the ram face of the spacecraft, the lowest in the wake, and intermediate values on the side. This indicates that the servicer is more likely to passively detect the target's potential near the ram or side of the spacecraft.

On all faces, the secondary electron yield is approximately the same, so the energy of the electrons to the spacecraft surfaces remains constant. The difference in emissions occurs due to differences in impacting electron current across the spacecraft surfaces. Nascap-2k shows this variation in the solar wind wake for altitudes above 12,000 km, where the spacecraft wake is largest. However, in all other regions the secondary electron current is uniform across all surfaces, indicating that Nascap-2k only accounts for current collection in mesothermal plasma when large spacecraft wake formations (wakes greater than several times the spacecraft width) occur.

Once again, barrier formations are not observed for the 2 m spacecraft because it is significantly smaller than the electron Debye lengths. In addition, non-monotonic sheaths form when the ratio of outgoing to incoming electrons Γ exceeds a critical value Γ_c. An approximation of this critical value can be found as[73]

$$\Gamma_c = 1 - 8.3\sqrt{\frac{m_e}{m_i}}, \tag{5}$$

where m_e is the mass of an electron (m_e ≈9.1E-13 kg) and m_i is the ion mass. Hydrogen ions H^+ are assumed in this project (m_i ≈1.67E-27 kg), so the critical ratio is approximately 0.81.

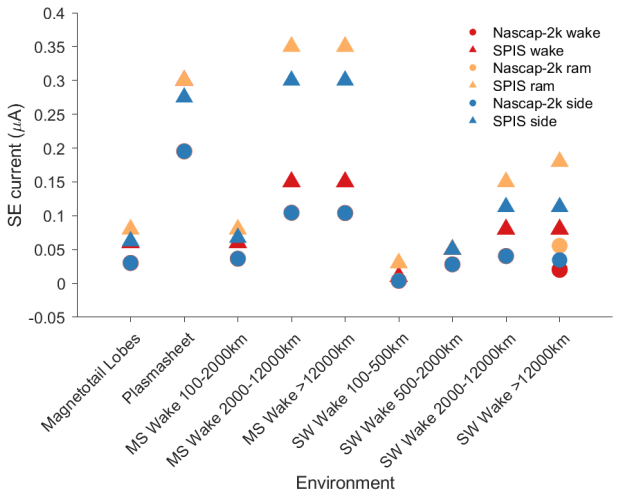

Figure 6. Secondary electron currents on the the ram, wake, and side of the spacecraft in eclipse cislunar environments.

In the solar wind wake environment at altitudes above 12,000 km, with secondary electron yield properties defined in the Current Sources section, the calculated Γ is around 0.3. So, barriers due to secondary electrons are not expected to form regardless of spacecraft size. To generate a barrier formation, simulations are also conducted with modified secondary electron yield parameters. The R_1, R_2, e_1, and e_2 variables from Equation (3) are held the same, and the maximum yield and energy at which the maximum yield occurs are changed to 1.25 and 200 eV, respectively, generating a Γ of approximately 0.89.

Figure 7 shows the potential sheaths and secondary electron density about 10 m spacecraft with and without a secondary electron barrier. Without a barrier, the potential field decreases monotonically, repelling the secondary electrons from the negative spacecraft. With a barrier, there is a potential dip around the entire spacecraft due to the secondary electrons, and an even more negative region inside the wake. The secondaries then form a sheath surrounding the spacecraft instead of simply being repelled. Previous work has shown that secondary electron trajectories are highly dependent on target geometry, which limits the regions in which secondaries can be detected around a target spacecraft.[17,18,74–76] However, if the presence of a barrier creates a nearly sheath of electrons around a target, it may actually be easier for the servicer to find electron emissions if it is capable of pulling electrons through the barrier. The exception may be on the wake side of the target, where it can be seen that the secondary electron density is lower.

Figure 8 shows the potential fields around spacecraft of varying sizes with and without sufficient secondaries to generate a barrier. Interestingly, there is not a barrier due to the wake for the spacecraft with a lower secondary electron yield. It is possible that the spacecraft is more negative than the potential field wake region, preventing barrier formation. Future research could explore the potentials in which wake barriers form. When the secondary electron yield is higher, a non-monotonic sheath clearly forms on both the ram and wake side of the spacecraft when the spacecraft is 6 m wide($\rho \approx 0.29$). This is a smaller ratio that what is required for non-monotonic sheaths to form due to photoelectrons. This may be due to the smaller spacecraft potentials in this scenario compared to those in Figure 5(a). Once again, the barrier is more negative in the wake region, and, as shown in

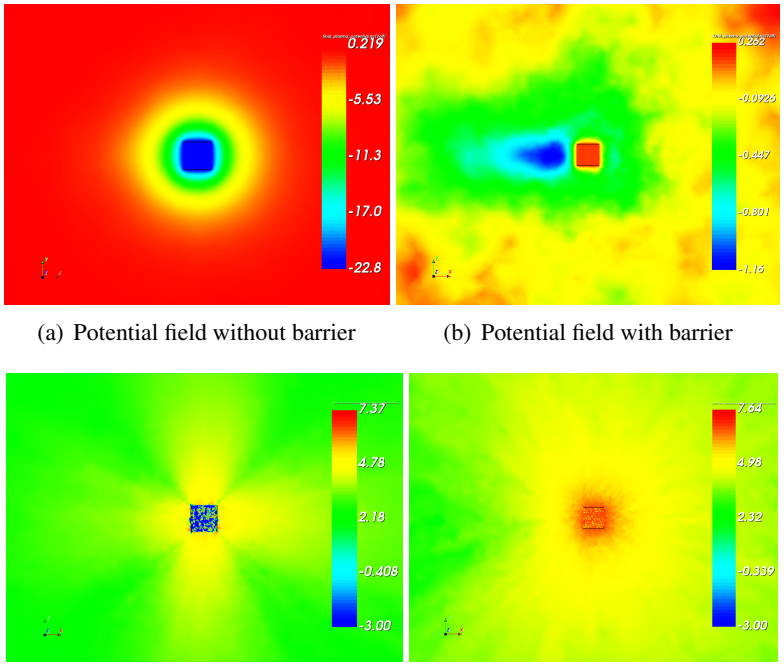

(a) Potential field without barrier (b) Potential field with barrier

(c) $\log_{10}(n_{se})$ without barrier (d) $\log_{10}(n_{se})$ with barrier

Figure 7. The potential field (top) and $\log_{10}$ of the secondary electron density n_{se} (bottom) for a 10 m spacecraft without a barrier formation (left) and with a barrier formation (right) in solar wind wake greater than 12,000 km altitude plasma (λ_D=20.5 m)

Figure 8(c), the secondary electron current is highest on the ram face and lowest in the wake. Furthermore, the current density on all faces decreases as the spacecraft size increases and minimum potential around the spacecraft becomes more negative.

PASSIVE POTENTIAL SENSING SIMULATIONS

The conditions in which passive potential sensing can be conducted is split into four scenarios based on the single spacecraft results: (1) sunlit with a barrier, (2) sunlit without a barrier, (3) eclipse with a barrier, and (4) eclipse without a barrier. Passive potential sensing simulations are conducted to determine the impact of barriers on sensing and the ideal servicer position with respect to the target. Simulations are conducted in Nascap-2k and SPIS for scenarios where barriers do not form to validate the models. When barriers are present, simulations are conducted only in SPIS because Nascap-2k does not capture non-monotonic sheath formations.

Because it was previously shown that the formation of barriers depends on the spacecraft width, the spacecraft size is also varied in touchless potential sensing simulations. In each case, the size of the target and servicer are set equal. Previous work has shown that the servicer's potential field accelerates the ambient electrons.[32] To increase the target's secondary electron emissions, the servicer's potential is held at 300 V, the energy corresponding to the maximum secondary electron yield. This could be achieved through spacecraft potential controls such as biasing of electric field sensors[77] and electron gun emissions.[15,78,79] The target is allowed to float, and the surface potential is determined by the current balance given in Equation (2). The resolution is the same as described

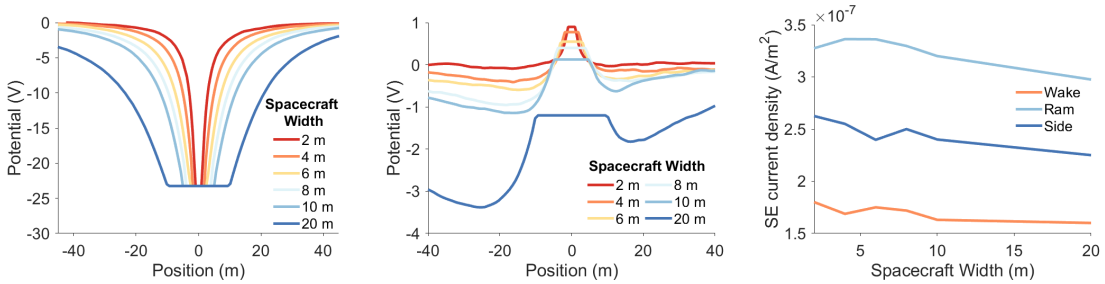

(a) Potential field without barrier (b) Potential field with barrier (c) SE current density

Figure 8. Potential fields about spacecraft without a barrier (left) and with a barrier (middle), and the secondary electron current density (right) for spacecraft of varying widths in solar wind wake greater than 12,000 km altitude plasma (λ_D=20.5 m). Fixed text size

in the Simulation Setup section.

The servicer and target are modeled in three relative positions: servicer in the target's wake (servicer eclipsed), target in the servicer's wake (target eclipsed), and servicer and target wakes parallel (both spacecraft sunlit). This provides insight into the servicer position changes the target's potential and emissions, and which position allows the servicer to detect the maximum electron emission current. The surface-to-surface separation distance is fixed at 10 m for all scenarios. It is assumed that an RPA is used to detect electron emissions that is located on the side of the servicer facing the target.

Sunlit Spacecraft

The spacecraft are initially modeled in the solar wind dayside environment, where non-monotonic sheaths form due to photoelectron emissions and the spacecraft wake when ρ is at least 0.59. Simulations utilize 2 m spacecraft ($\rho \approx 0.20$) to study sensing without barriers and 10 m spacecraft ($\rho \approx 0.99$) for sensing with a barrier. Based on the single spacecraft characterization, it is expected that positioning the servicer the side of the target would be ideal because this maximizes the detected photoelectron and secondary electron currents.

Table 2 shoes the final potential, emitted current, and detected current. For the 2 m servicer, the highest current is detected when the servicer is near the side of the target with neither spacecraft eclipsed. In this location, the servicer is able to attract the photoelectron current emitted from the target, as shown in Figure 9(b). The secondary electron current is detected as well, but it is orders of magnitude smaller than the photoelectron current. Unexpectedly, the next best position is when the servicer eclipsed by the target, as the servicer is actually able to attract the photoelectron emissions from the side of the target opposite the servicer (Figure 9(a)). The least effective position is with the target in the servicer's wake because the target does not emit the large photoelectron current and charges negatively. The negative charge repels most incoming electrons, reducing secondary electron emissions.

The photoelectron currents are larger in SPIS than Nascap-2k, likely because Nascap-2k underestimates the influence of the 300 V servicer on the photoelectron trajectories. As a result, less photoelectrons are pulled towards the servicer and instead re-enter the target's surface. Additionally, when the target is shadowed by the servicer and only secondary electrons are emitted, SPIS

Table 2. Passive potential sensing results for a sunlit environment.

Servicer size and position	SPIS Potential (V)	Nascap Potential (V)	SPIS Emitted Current (I/m^2)	Nascap Emitted Current (I/m^2)	SPIS Detected Current (I/m^2)	Nascap Detected Current (I/m^2)
2 m servicer, target eclipsed	-70	-26.9	0	9.2E-9	0	1.5E-9
2 m servicer, servicer eclipsed	23	4.4	7.7E-6	4.4E-6	9.4E-7	4.2E-8
2 m servicer, neither eclipsed	35	4.4	1.0E-5	4.5E-6	7.3E-6	8.4E-8
10 m servicer, target eclipsed	-102	N/A	0	N/A	0	N/A
10 m servicer, servicer eclipsed	18.5	N/A	1.0E-6	N/A	3.6E-7	N/A
10 m servicer, neither eclipsed	43	N/A	1.3E-5	N/A	3.4E-7	N/A

produces a more negative target potential and no secondary electron currents. This is likely due to differences in the wake formation. As shown in Figure 10, the wake is larger in SPIS and fully envelopes the target, which causes more extreme charging.[7] The more negative target then repels more ambient electrons and emits less secondaries, causing the difference in secondary electron current in Nascap-2k and SPIS. These findings indicate that even when the spacecraft is smaller than the electron Debye length, spacecraft formation significantly affects charging and sensing.

Now that the sensing process without barriers has been modeled in Nascap-2k and SPIS and both tools have shown the same trends, passive sensing in the presence of barriers is modeled in SPIS. As shown in Figure 9(c), the servicer is again able to attract photoelectron emissions when it is located in the target's wake, indicating that the servicer is able to overcome the photoemission barrier. Approximately 87% of the photoelectron density is recollected by the target, while 91% of the photoelectron density was recollected when the target was modeled without the servicer present. This validates that the servicer is pulling the photoelectron emissions away from the target. Furthermore, the non-monotonic sheath does not form around the target. This likely occurs because the servicer causes the target to charge more positive, and non-monotonic sheath formation can change to monotonic sheaths if the spacecraft potential is sufficiently positive.[80] Therefore, a positively charged servicer can be utilized to overcome barriers due to non-monotonic sheaths.

The target recollects less of its current when neither spacecraft are eclipsed, but the servicer detects about the same current as when the target is eclipsing the servicer. Figure 9(d) shows that the emitted photoelectrons are mostly attracted to the side of the servicer that does not have the RPA, whereas the smaller spacecraft in Figure 9(b) shows the photoelectrons surrounding the servicer. This may occur because the separation distance to spacecraft width ratio is smaller, with the 2 m spacecraft separated by 5 spacecraft widths while the 10 m spacecraft are a singular spacecraft width apart. Future simulations with 10 m spacecraft separated by 50 m may be conducted to validate this. Regardless, the non-monotonic sheath again does not form, indicating again that a positively charged servicer can be utilized to overcome barriers.

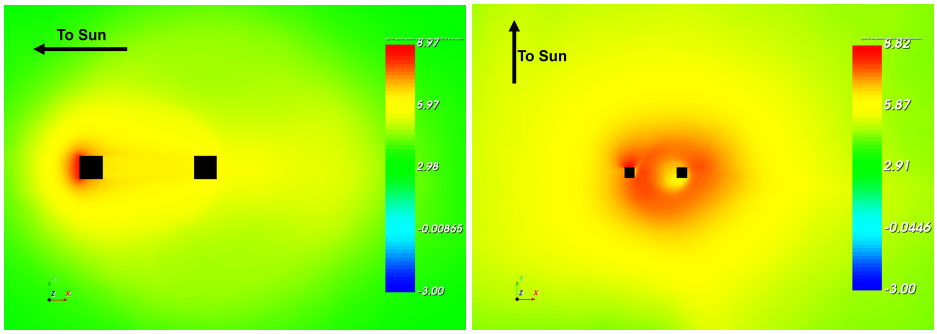

(a) 2 m servicer in target's wake (b) 2 m spacecraft with parallel wakes

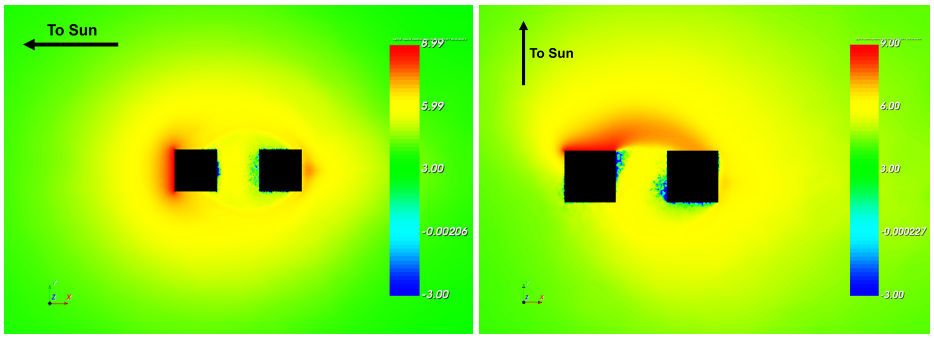

(c) 10 m servicer in target's wake (d) 10 m spacecraft with parallel wakes

Figure 9. $\log_{10}$ of the photoelectron density about a servicer (right) and target (left) in the solar wind dayside environment.

The target again emits no electron current when it is eclipsed by the servicer because the target charges highly negative and repels the ambient electrons. If the target is farther from the servicer, it is possible that it will charge less negative, allowing the target to emit secondary electrons. Future work will be conducted to determine how the separation distance influences the sensing process.

Eclipsed Spacecraft

The spacecraft are now modeled in the solar wind wake environment at an altitude above 12,000 km. Here, non-monotonic sheaths are expected to form when ρ is greater than 0.29 and Γ is greater than Γ_c ($\approx$0.81). Based on the single spacecraft characterization, it is expected that positioning the servicer on the ram or side of the target will be best for sensing. It was shown in the previous section that the same trends are demonstrated in Nascap-2k and SPIS, so sensing is investigated only using SPIS in this section.

Table 3 shows the final potential, emitted current from the target, and detected current. The ideal position, regardless of secondary electron yield, is when the servicer and target's wakes are parallel. This follows the expectations from the individual spacecraft results. The worst is when the target is in the servicer's wake. This again likely occurs because the target charges more negatively, repelling ambient electrons and emitting less secondary electrons. Placing the servicer in the target's wake yields similar results to when the wakes are parallel because the servicer is able to draw the secondary electron emissions from the target. This is validated in Figures 11(b) and 11(c), as the secondary electron density is nearly identical in the two scenarios.

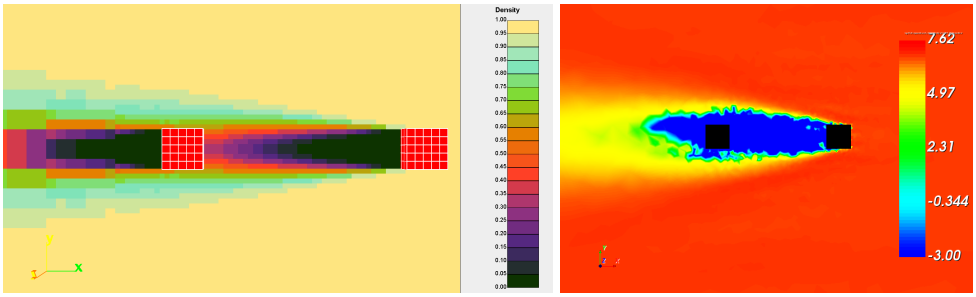

(a) Nascap-2k neutral wake (b) SPIS ion density

Figure 10. Wake formation in the solar wind dayside region when the target is in the servicer's wake shown with the neutral wake in Nascap-2k (left) and ion density in SPIS (right).

Table 3. Passive potential sensing results for an eclipsed environment.

Barrier/no barrier and position	**SPIS Potential (V)**	**SPIS Emitted Current (I/m^2)**	**SPIS Detected Current (I/m^2)**
No barrier, target in wake	-62.5	2.7E-8	1.3E-9
No barrier, servicer in wake	-18.5	1.8E-7	5E-9
No barrier, parallel wakes	-20	1.9E-7	7E-9
Barrier, target in wake	-57	5.5E-8	4.9E-9
Barrier, servicer in wake	-7.8	3.1E-7	2E-8
Barrier, parallel wakes	-8.2	4.1E-7	2.3E-8

When the secondary electron yield is increased such that Γ is greater than Γ_c and a barrier is expected to form about the target, non-monotonic sheaths do not form around the target. This again can be contributed to the positive servicer. The secondary electron density shown in Figure 11 demonstrates this, as the secondaries appear to follow similar trajectories both when $\Gamma < \Gamma_c$ and $\Gamma > \Gamma_c$. Therefore, barriers due to secondary electron trajectories do not pose an issue to touchless potential sensing when the servicer is held significantly positive.

CONCLUSION

Spacecraft charging trends and barriers due to wake formations and non-monotonic sheaths are characterized using Nascap-2k and SPIS. It is shown that increasing the spacecraft size causes the system to transition from the thick sheath to thin sheath regime, allowing barriers to form around the spacecraft. These formations limit the electron current that leaves the target, making touchless potential sensing using passive methods more difficult. The results also indicate the possibility of a relationship between the spacecraft potential and barrier formation, as barriers do not form when the spacecraft potential is sufficiently large. This will be investigated in future research.

With the trends characterized, passive potential sensing simulations are conducted with a 300 V servicer. It is shown that in both eclipse and sunlight, the best servicer position is near the side of the target when neither spacecraft are in the other's wake. The worst position in all scenarios is when the target is in the servicer's wake. In the wake, the target charges significantly more negative,

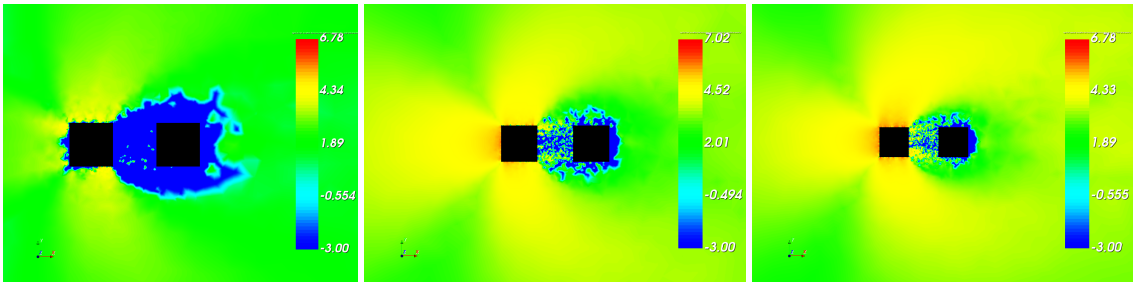

(a) Target in servicer's wake, $\Gamma < \Gamma_c$ (b) Servicer in target's wake, $\Gamma < \Gamma_c$ (c) Parallel wakes, $\Gamma < \Gamma_c$

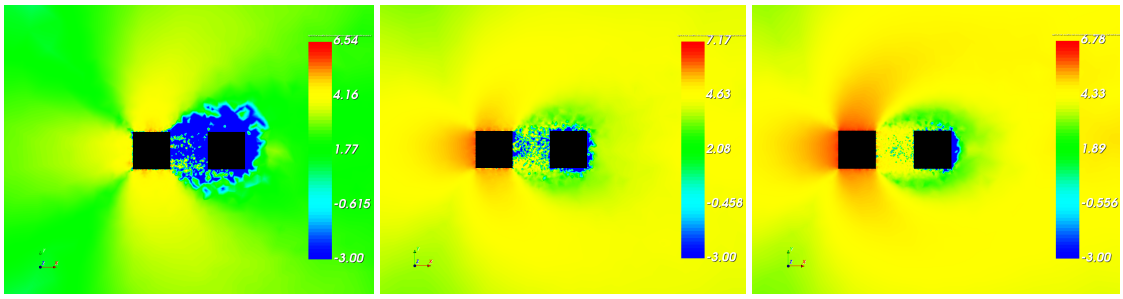

(d) Target in servicer's wake, $\Gamma > \Gamma_c$ (e) Servicer in target's wake, $\Gamma > \Gamma_c$ (f) Parallel wakes, $\Gamma > \Gamma_c$

Figure 11. $\log_{10}$ of the secondary electron density about a servicer (right) and target (left) in the solar wind wake environment above 12,000 km.

repelling nearly all ambient electrons and emitting little secondary electron current. It is possible that larger separation distances will enable sensing in this configuration, and this is left for future work.

In addition, it is shown that the presence of a highly positive servicer near the target causes the barrier formations to disappear, enabling passive touchless potential even in scenarios where electron emissions are not initially expected to leave the target's surface.

ACKNOWLEDGMENTS

This work is supported by a NASA Space Technology Graduate Research Opportunity Grant Number 80NSSC22K1175. The authors would like to thank Emily Willis for her advice on properly running the SPIS simulations.

REFERENCES

[1] S. T. Lai, *Fundamentals of Spacecraft Charging: Spacecraft Interactions with Space Plasmas*. Princeton University Press, 2012.

[2] K. Balmain, "Arc propagation, emission and damage on spacecraft dielectrics: A review," *Journal of electrostatics*, Vol. 20, No. 1, 1987, pp. 95–108.

[3] J. A. Roth, *Electrostatic Discharge in Spacecraft Materials*. PhD thesis, Utah State University, 2009.

[4] S. T. Lai, K. Cahoy, W. Lohmeyer, A. Carlton, R. Aniceto, and J. Minow, "Deep dielectric charging and spacecraft anomalies," *Extreme events in Geospace*, pp. 419–432, Elsevier, 2018.

[5] Y. Xiangqian, C. Hongfei, Z. Qiugang, W. Jianzhao, S. Weihong, Z. Hong, Z. Jiqing, Z. Weiying, C. Zhe, S. Sipei, *et al.*, "Mitigating deep dielectric charging effects in space," *IEEE Transactions on Nuclear Science*, Vol. 64, No. 11, 2017, pp. 2822–2828.

[6] X. Yu, S. Song, H. Chen, Y. Qu, H. Zou, Q. Zong, W. Shi, J. Zou, W. Zhong, H. Xiang, *et al.*, "Monitoring deep dielectric charging effects in space," *IEEE Transactions on Nuclear Science*, Vol. 67, No. 4, 2019, pp. 716–721.

[7] J. Wang, P. Leung, H. Garrett, and G. Murphy, "Multibody-plasma interactions-Charging in the wake," *Journal of Spacecraft and Rockets*, Vol. 31, No. 5, 1994, pp. 889–894.

[8] M. McCollum, E. Willis, and A. Diekmann, "Artemis IV Docking in Radiation Belt Charging Environment," *Applied Space Environments Conference 2023*, Huntsville, AL, Aug. 2023.

[9] E. Willis, A. Diekmann, and M. Guy, "Plasma Charging of Crewed Spacecraft in Lunar Orbit," *Space Environment Engineering and Science Applications Workshop*, Laurel, MD, Sept. 2022.

[10] K. Wilson, A. Romero-Calvo, and H. Schaub, "Constrained Guidance for Spacecraft Proximity Operations Under Electrostatic Perturbations," *Journal of Spacecraft and Rockets*, Vol. 0, No. 0, 2022, pp. 1–13. *in press*, 10.2514/1.A35162.

[11] J. Hammerl and H. Schaub, "Effects of Electric Potential Uncertainty on Electrostatic Tractor Relative Motion Control Equilibria," *Journal of Spacecraft and Rockets*, Vol. 59, No. 2, 2022, pp. 552–562, 10.2514/1.A35165.

[12] M. Bengtson, K. Wilson, J. Hughes, and H. Schaub, "Survey of the electrostatic tractor research for reorbiting passive GEO space objects," *Astrodynamics*, Vol. 2, Dec 2018, pp. 291–305.

[13] J. A. Hughes and H. Schaub, "Electrostatic Tractor Analysis Using a Measured Flux Model," *Journal of Spacecraft and Rockets*, Vol. 57, No. 2, 2020, pp. 207–216.

[14] E. A. Hogan and H. Schaub, "Impacts Of Tug And Debris Sizes On Electrostatic Tractor Charging Performance," *Advances in Space Research*, Vol. 55, January 15 2015, pp. 630–638, 10.1016/j.asr.2014.10.023.

[15] E. A. Hogan and H. Schaub, "Impacts of Hot Space Plasma and Ion Beam Emission on Electrostatic Tractor Performance," *IEEE Transactions on Plasma Science*, Vol. 43, Sept. 2014, pp. 3115–3129, 10.1109/TPS.2015.2451001.

[16] M. Bengtson, J. Hughes, and H. Schaub, "Prospects and Challenges for Touchless Sensing of Spacecraft Electrostatic Potential Using Electrons," *IEEE Transactions on Plasma Science*, Vol. 47, No. 8, 2019, pp. 3673–3681.

[17] M. T. Bengtson and H. Schaub, "Electron-Based Touchless Potential Sensing of Shape Primitives and Differentially-Charged Spacecraft," *Journal of Spacecraft and Rockets*, Vol. 58, Nov. – Dec. 2021, pp. 1847–1857, 10.2514/1.A35086.

[18] M. T. Bengtson, K. T. Wilson, and H. Schaub, "Experimental Results of Electron Method for Remote Spacecraft Charge Sensing," *Space Weather*, Vol. 18, No. 3, 2020, pp. 1–12, 10.1029/2019SW002341.

[19] A. R. Calvo, J. Hammerl, and H. Schaub, "Touchless potential sensing of complex differentially-charged shapes using secondary electrons," *AIAA SCITECH 2022 Forum*, 2022, 10.2514/6.2022-2311.

[20] K. T. H. Wilson and H. Schaub, "X-Ray Spectroscopy for Electrostatic Potential and Material Determination of Space Objects," *IEEE Transactions on Plasma Science*, Vol. 47, Aug. 2019, pp. 3858–3866, 10.1109/TPS.2019.2910576.

[21] K. T. Wilson, M. T. Bengtson, and H. Schaub, "X-ray Spectroscopic Determination of Electrostatic Potential and Material Composition for Spacecraft: Experimental Results," *Space Weather*, Vol. 18, No. 4, 2020, p. e2019SW002342, 10.1029/2019SW002342.

[22] J. Hammerl, A. López, A. Romero Calvo, and H. Schaub, "Touchless Potential Sensing of Differentially Charged Spacecraft Using X-Rays," *Journal of Spacecraft and Rockets*, Vol. 60, March–April 2023, pp. 648–658, 10.2514/6.2022-2312.

[23] A. Romero Calvo, K. Champion, and H. Schaub, "Enabling Ultraviolet Lasers for Touchless Spacecraft Potential Sensing," *IEEE Transactions on Plasma Science*, Vol. 51, Sept. 2023, pp. 2468–2481, 10.1109/TPS.2023.3264914.

[24] K. T. H. Wilson, J. Hammerl, and H. Schaub, "Using Plasma-Induced X-Ray Emission to Estimate Electrostatic Potentials on Nearby Space Objects," *Journal of Spacecraft and Rockets*, Vol. 59, July–Aug. 2022, pp. 1402–1405, 10.2514/1.A35161.

[25] S. T. Lai and C. Miller, "Retarding potential analyzer: Principles, designs, and space applications," *AIP Advances*, Vol. 10, No. 9, 2020, p. 095324, 10.1063/5.0014266.

[26] R. Schmidt, H. Arends, A. Pedersen, F. Rüdenauer, M. Fehringer, B. T. Narheim, R. Svenes, K. Kvernsveen, K. Tsuruda, T. Mukai, H. Hayakawa, and M. Nakamura, "Results from active spacecraft potential control on the Geotail spacecraft," *Journal of Geophysical Research: Space Physics*, Vol. 100, No. A9, 1995, pp. 17253–17259, https://doi.org/10.1029/95JA01552.

[27] L. Goembel and J. P. Doering, "Instrument for measuring spacecraft potential," *Journal of Spacecraft and Rockets*, Vol. 35, No. 1, 1998, pp. 66–72, 10.2514/3.26999.

[28] S. Mathavaraj and K. Negi, "Chandrayaan-3 Trajectory Design: Injection to Successful Landing," *Journal of Spacecraft and Rockets*, 2024, pp. 1–8.

[29] C. Li, H. Hu, M.-F. Yang, J. Liu, Q. Zhou, X. Ren, B. Liu, D. Liu, X. Zeng, W. Zuo, G. Zhang, H. Zhang, S. Yang, Q. Wang, X. Deng, X. Gao, Y. Su, W. Wen, and Z. Ouyang, "Nature of the lunar farside samples returned by the Chang'E-6 mission," *National Science Review*, 09 2024, p. nwae328, 10.1093/nsr/nwae328.

[30] S. Ueda, T. Ito, and S.-i. Sakai, "A study on guidance technique for precise lunar landing," *Proceedings of 31st ISTS*, 2017.

[31] S. Creech, J. Guidi, and D. Elburn, "Artemis: an overview of NASA's activities to return humans to the Moon," *2022 ieee aerospace conference (aero)*, IEEE, 2022, pp. 1–7.

[32] K. Champion and H. Schaub, "Electrostatic Potential Shielding in Representative Cislunar Regions," *IEEE Transactions on Plasma Science*, Vol. 51, Sept. 2023, pp. 2482–2500, 10.1109/TPS.2023.3236246.

[33] K. Anderson, L. Chase, R. Lin, J. McCoy, and R. McGuire, "Solar-wind and interplanetary electron measurements on the Apollo 15 subsatellite," *Journal of Geophysical Research*, Vol. 77, No. 25, 1972, pp. 4611–4626.

[34] E. Zinner, R. Walker, J. Borg, and M. Maurette, "Measurement of heavy solar wind particles during the Apollo 17 mission," *Conference on Solar Wind Three 3*, Non Mentionne, 1974, pp. 27–32.

[35] J. Geiss, P. Eberhardt, F. Bühler, J. Meister, and P. Signer, "Apollo 11 and 12 solar wind composition experiments: Fluxes of He and Ne isotopes," *Journal of Geophysical Research*, Vol. 75, No. 31, 1970, pp. 5972–5979.

[36] K. Ogilvie and M. Desch, "The WIND spacecraft and its early scientific results," *Advances in Space Research*, Vol. 20, No. 4, 1997, pp. 559–568. Results of the IASTP Program, https://doi.org/10.1016/S0273-1177(97)00439-0.

[37] R. Vondrak, J. Keller, G. Chin, and J. Garvin, "Lunar Reconnaissance Orbiter (LRO): Observations for lunar exploration and science," *Space science reviews*, Vol. 150, 2010, pp. 7–22.

[38] V. Angelopoulos, "The ARTEMIS mission," *The ARTEMIS mission*, 2014, pp. 3–25.

[39] F. B. Leahy, "SLS-SPEC-159, Cross-Program Design Specification for Natural Environments (DSNE)," tech. rep., National Aeronautics and Space Administration, 2021.

[40] J. Halekas, Y. Saito, G. Delory, and W. Farrell, "New views of the lunar plasma environment," *Planetary and Space Science*, Vol. 59, No. 14, 2011, pp. 1681–1694. Lunar Dust, Atmosphere and Plasma: The Next Steps, https://doi.org/10.1016/j.pss.2010.08.011.

[41] J. Wang and D. Hastings, "Ionospheric plasma flow over large high-voltage space platforms. I: Ion-plasma–time scale interactions of a plate at zero angle of attack," *Physics of Fluids B: Plasma Physics*, Vol. 4, No. 6, 1992, pp. 1597–1614.

[42] J. Wang and D. Hastings, "Ionospheric plasma flow over large high-voltage space platforms. II: The formation and structure of plasma wake," *Physics of Fluids B: Plasma Physics*, Vol. 4, No. 6, 1992, pp. 1615–1629.

[43] Y. Hu and J. Wang, "Plasma Wake Simulation for Charged Space Platforms: Fully Kinetic PIC Versus Hybrid PIC," *IEEE Transactions on Plasma Science*, Vol. 47, No. 8, 2019, pp. 3731–3738.

[44] N. Ahmad, H. Usui, and Y. Miyake, "The Particle-In-Cell simulation on LEO spacecraft charging and the wake structure using EMSES," *Journal of Advanced Simulation in Science and Engineering*, Vol. 6, No. 1, 2019, pp. 21–31.

[45] W. Miloch, V. Yaroshenko, S. Vladimirov, H. Pécseli, and J. Trulsen, "Spacecraft charging in flowing plasmas; numerical simulations," *Journal of Physics: Conference Series*, Vol. 370, IOP Publishing, 2012, p. 012004.

[46] A. Sjogren, A. I. Eriksson, and C. M. Cully, "Simulation of potential measurements around a photoemitting spacecraft in a flowing plasma," *IEEE Transactions on Plasma Science*, Vol. 40, No. 4, 2012, pp. 1257–1261.

[47] Y. Miyake, C. Cully, H. Usui, and H. Nakashima, "Plasma particle simulations of wake formation behind a spacecraft with thin wire booms," *Journal of Geophysical Research: Space Physics*, Vol. 118, No. 9, 2013, pp. 5681–5694.

[48] J. Maxwell and H. Schaub, "Low Earth Orbit Plasma Wake Shaping and Applications to On-Orbit Proximity Operations," *IEEE Transactions on Plasma Science*, Vol. 47, No. 10, 2019, pp. 4760–4769, 10.1109/TPS.2019.2939712.

[49] W. Oran, U. Samir, N. H. Stone, and E. Fontheeim, "Laboratory observations of electron temperature in the wake of a sphere in a streaming plasma," *Planetary and Space Science*, Vol. 23, No. 7, 1975, pp. 1081–1083.

[50] S. Raychaudhuri, J. Hill, H. Y. Chang, E. K. Tsikis, and K. E. Lonngren, "An experiment on the plasma expansion into a wake," *The Physics of Fluids*, Vol. 29, 01 1986, pp. 289–293, 10.1063/1.865994.

[51] K. Svencs and J. Trøim, "Laboratory simulation of vehicle-plasma interaction in low Earth orbit," *Planetary and space science*, Vol. 42, No. 1, 1994, pp. 81–94.

[52] S. Hester and A. A. Sonin, "A laboratory study of the wakes of ionospheric satellites," *AIAA Journal*, Vol. 8, No. 6, 1970, pp. 1090–1098.

[53] C. Enloe, D. Cooke, S. Meassick, C. Chan, and M. Tautz, "Ion collection in a spacecraft wake: Laboratory simulations," *Journal of Geophysical Research: Space Physics*, Vol. 98, No. A8, 1993, pp. 13635–13644.

[54] R. Biasca and J. Wang, "Ion current collection in spacecraft wakes," *Physics of Plasmas*, Vol. 2, 01 1995, pp. 280–288, 10.1063/1.871098.

[55] W. Yu, J. Wang, and K. Chou, "Laboratory Measurement of Lunar Regolith Simulant Surface Charging in a Localized Plasma Wake," *IEEE Transactions on Plasma Science*, Vol. 43, No. 12, 2015, pp. 4175–4181, 10.1109/TPS.2015.2492551.

[56] K. Champion and H. Schaub, "Feasibility of Cislunar Spacecraft Wake Generation," *AIAA SciTech*, National Harbor, Maryland, January 23–28 2023.

[57] R. E. Ergun, D. M. Malaspina, S. D. Bale, J. P. McFadden, D. E. Larson, F. S. Mozer, N. Meyer-Vernet, M. Maksimovic, P. J. Kellogg, and J. R. Wygant, "Spacecraft charging and ion wake formation in the near-Sun environment," *Physics of Plasmas*, Vol. 17, 07 2010, p. 072903, 10.1063/1.3457484.

[58] S. Guillemant, V. Génot, J.-C. Matéo-Vélez, R. Ergun, and P. Louarn, "Solar wind plasma interaction with solar probe plus spacecraft," *Annales Geophysicae*, Vol. 30, Copernicus Publications Göttingen, Germany, 2012, pp. 1075–1092.

[59] S. Guillemant, V. Génot, J.-C. M. Vélez, P. Sarrailh, A. Hilgers, and P. Louarn, "Simulation Study of Spacecraft Electrostatic Sheath Changes With the Heliocentric Distances From 0.044 to 1 AU," *IEEE Transactions on Plasma Science*, Vol. 41, No. 12, 2013, pp. 3338–3348, 10.1109/TPS.2013.2246193.

[60] J. Deca, G. Lapenta, R. Marchand, and S. Markidis, "Spacecraft charging analysis with the implicit particle-in-cell code iPic3D," *Physics of Plasmas*, Vol. 20, No. 10, 2013.

[61] H. Zhao, R. Schmidt, C. Escoubet, K. Torkar, and W. Riedler, "Self-consistent determination of the electrostatic potential barrier due to the photoelectron sheath near a spacecraft," *Journal of Geophysical Research: Space Physics*, Vol. 101, No. A7, 1996, pp. 15653–15659.

[62] X. Wang, H.-W. Hsu, and M. Horányi, "Identification of when a Langmuir probe is in the sheath of a spacecraft: The effects of secondary electron emission from the probe," *Journal of Geophysical Research: Space Physics*, Vol. 120, No. 4, 2015, pp. 2428–2437.

[63] T. Burinskaya, "Non-monotonic potentials above the day-side lunar surface exposed to the solar radiation," *Planetary and Space Science*, Vol. 115, 2015, pp. 64–68.

[64] J. Zhao, X. Wei, X. Du, X. He, and D. Han, "Photoelectron sheath and plasma charging on the lunar surface: Semianalytic solutions and fully-kinetic particle-in-cell simulations," *IEEE Transactions on Plasma Science*, Vol. 49, No. 10, 2021, pp. 3036–3050.

[65] T. Sana and S. Mishra, "Plasma Sheath around Chandrayaan-3 Landing Site: A Case Study," *The Planetary Science Journal*, Vol. 4, No. 9, 2023, p. 158.

[66] X. Wang, J. Pilewskie, H.-W. Hsu, and M. Horányi, "Plasma potential in the sheaths of electron-emitting surfaces in space," *Geophysical Research Letters*, Vol. 43, No. 2, 2016, pp. 525–531.

[67] V. T. Gurovich, J. Gleizer, Y. Bliokh, and Y. E. Krasik, "Potential distribution in an ion sheath of non-Maxwellian plasma," *Physics of plasmas*, Vol. 13, No. 7, 2006.

[68] A. Poppe, J. S. Halekas, and M. Horányi, "Negative potentials above the day-side lunar surface in the terrestrial plasma sheet: Evidence of non-monotonic potentials," *Geophysical Research Letters*, Vol. 38, No. 2, 2011, https://doi.org/10.1029/2010GL046119.

[69] M. J. Mandell, V. A. Davis, D. L. Cooke, A. T. Wheelock, and C. J. Roth, "Nascap-2k spacecraft charging code overview," *IEEE Transactions on Plasma Science*, Vol. 34, No. 5, 2006, pp. 2084–2093.

[70] P. Sarrailh, J.-C. Matéo-Vélez, S. L. G. Hess, J.-F. Roussel, B. Thiébault, J. Forest, B. Jeanty-Ruard, A. Hilgers, D. Rodgers, F. Cipriani, and D. Payan, "SPIS 5: New Modeling Capabilities and Methods for Scientific Missions," *IEEE Transactions on Plasma Science*, Vol. 43, No. 9, 2015, pp. 2789–2798, 10.1109/TPS.2015.2445384.

[71] V. A. Davis and M. J. Mandell, "NASCAP-2K VERSION 4.3 SCIENTIFIC DOCUMENTATION," Technical Report AFRL-RV-PS-TR-2017-0001, Dec. 2016.

[72] D. Tskhakaya, K. Matyash, R. Schneider, and F. Taccogna, "The Particle-In-Cell Method," *Contributions to Plasma Physics*, Vol. 47, No. 8-9, 2007, pp. 563–594.

[73] G. Hobbs and J. Wesson, "Heat flow through a Langmuir sheath in the presence of electron emission," *Plasma Physics*, Vol. 9, No. 1, 1967, p. 85.

[74] K. T. Wilson, M. Bengtson, and H. Schaub, "Remote Electrostatic Potential Sensing for Proximity Operations: Comparison and Fusion of Methods," *Journal of Spacecraft and Rockets*, 2021. *under review*.

[75] A. Romero Calvo, J. Hammerl, and H. Schaub, "Touchless Potential Sensing of Complex Differentially-Charged Shapes Using Secondary Electrons," *AIAA Journal of Spacecraft and Rockets*, Vol. 59, Sept. – Oct. 2022, pp. 1623–1633, 10.2514/1.A35355.

[76] K. M. Champion, A. Romero-Calvo, and H. Schaub, "Large scale particle tracing simulation for touchless potential sensing," *AIAA SCITECH 2023 Forum*, 2023, p. 1770.

[77] J. Bonnell, F. Mozer, G. Delory, A. Hull, R. Ergun, C. Cully, V. Angelopoulos, and P. Harvey, "The electric field instrument (EFI) for THEMIS," *The THEMIS mission*, 2009, pp. 303–341.

[78] E. Hogan and H. Schaub, "Space Weather Influence on Relative Motion Control using the Touchless Electrostatic Tractor," *Journal of Astronautical Sciences*, Vol. 63, No. 3, 2016, pp. 237–262, 10.1007/s40295-016-0090-4.

[79] J. Hammerl and H. Schaub, "Coupled Spacecraft Charging Due to Continuous Electron Beam Emission and Impact," *Journal of Spacecraft and Rockets*, Vol. 0, No. 0, 0, pp. 1–14, 10.2514/1.A36010.

[80] B. Thiébault, A. Hilgers, E. Sasot, H. Laakso, P. Escoubet, V. Génot, and J. Forest, "Potential barrier in the electrostatic sheath around a magnetospheric spacecraft," *Journal of Geophysical Research: Space Physics*, Vol. 109, No. A12, 2004.